Learning Atom Probe Tomography time-of-flight peaks for mass-to-charge ratio spectrometry

Kevin J Coakley[1], Norman A Sanford

National Institute of Standards and Technology, 325 Broadway, Boulder CO 80305, USA

Abstract

In laser-assisted atom probe tomography, an important goal is to reconstruct the mass-to-charge ratio, (m/z), spectrum due to various ion species. In general, the probability mass function (pmf) associated with the time-of-flight (TOF) spectrum produced by each ion species is unknown and varies from species-to-species. Moreover, measuring pmfs for distinct ion species in calibration experiments is not practical. Here, we present a mixture model method to determine TOF pmfs that can vary from peak-to-peak. In this approach, we determine weights of candidate pmfs with a maximum likelihood method. In a proof-of-principle study, we apply our method to a TOF spectrum acquired from a silicon sample and determine intensity estimates of singly charged isotopes of silicon.

Keywords: Atom Probe Tomography, Cross-validation, Expectation Maximization algorithm, Machine learning, Maximum likelihood, Mixture model, Silicon isotopes

1. Introduction

In laser-assisted atom probe tomography (APT) [1, 2, 3, 4, 5], a sharp, needle-shaped specimen is subjected to an external electric field bias, which is held just below the threshold for field evaporation of ions. Field evaporation is triggered by incident laser pulses, imparting weak thermal transients, enabling the evaporation threshold to be exceeded. As a result, surface atoms

Email addresses: kevin.coakley@nist.gov (Kevin J Coakley), norman.sanford@nist.gov (Norman A Sanford)

[1]Corresponding author

originating from the vicinity of the specimen apex are evaporated (in the form of ions) synchronously with the laser pulses. The ions hit a 2-dimensional detector and their respective impact locations and times-of-flight are recorded. A back-projection algorithm applied to the accumulated data enables 3-D reconstruction of the specimen. This reconstruction locates and identifies each constituent species. Given the mass m and charge z of the ion, in the simplest approximation, the theoretical time-of-flight (transit time) of the ion to the detector, t, satisfies the following equation

$$\frac{m}{z} = \frac{2eV_{app}}{L^2}t^2, \tag{1}$$

where e is the charge of the electron, V_{app} is the bias voltage between the specimen and the electrode and L is the length of the ion trajectory, which is referred to as the flight length.

In actual experiments, the specimens are often conical so that the apex diameter gradually increases as ions are evaporated away and the specimen shortens. In this context, "apex diameter" refers to the diameter of a sphere which approximates the shape of a specimen apex. As the apex diameter increases, V_{app} is generally increased to maintain a constant evaporation field for a desired detection rate of ions. For conical specimens, the initial and final apex diameters are typically in the range of 20 nm and 150 nm, respectively; the length reduction of the specimen during an APT session is often a few hundred nm depending upon experimental targets. The specimen-electrode separation is roughly 30 μm to 40 μm. Now, if V_{app} is instead held constant, there is a negligible reduction in the evaporation field due only to the sample shortening and the apex receding from the electrode as ions are evaporated away; the increasing apex diameter is the dominant effect that influences the evaporation field when V_{app} is held constant. However, for a rod-like specimen of uniform diameter, V_{app} and the apex diameter, can both remain nearly constant throughout the APT run while still maintaining the desired detection rate [7]. In such a situation, V_{app} will rise solely because the apex retreats from the electrode as ions are lost from the specimen. An analysis of APT specimen apex electrostatics has been given by Zhang et al. [8].

In our experiments, the electrode-to-detector separation is 90 mm. Within the approximations leading to Eq. 1, variations in flight length due to the specimen-to-electrode separation, or due to an actual, originating, atomic location on or near the specimen apex, are considered negligible. The detector surface is a flat, circular region roughly 50 mm in diameter. As a conse-

quence of geometry therefore, the flight length, L, and corresponding TOF both depend upon where on the detector a detection event is registered; the minimum flight length being 90 mm.

For analysis, the TOF data are transformed so that an m/z peak, for example a 28-Da Si peak, will show the same apparent TOF over the entire swing of V_{app}. The data are further transformed so that the (physically) flat detector is transformed into a hypothetical hemispherical section so that an ion's apparent flight length will be independent of where it strikes the detector. These transformations of APT data are generally called "voltage" and "bowl" corrections [2, 3, 6]. Operationally, the voltage and bowl corrections are performed on raw TOF data with IVAS software [9]. After the voltage/bowl corrections, the TOF data are transformed to m/z data that is then calibrated with IVAS software based on recognized locations of m/z peaks for Si. Finally, the m/z data are transformed back to TOF data. We then scale this TOF data so that its sample mean agrees with the sample mean of the raw TOF data.

Due in part to thermal effects, the evaporation time of any ion and its TOF are both random. Hence, ions with particular m/z values produce temporal peaks that are broadened with respect to an idealized measurement where an ion evaporates within a time interval of 8 ps after the arrival of the laser pulse (which has a width of 8 ps). In the real situation, ions are persistently emitted at times greater than 8 ps after the arrival of the pulse since it takes time for the tip to cool below the threshold for field emission. In this work, we focus on the problem of reconstruction of the m/z spectrum of ions produced by laser energy deposits in a sample given a measured TOF spectrum produced by the evaporated ions.

In [10], the authors review how practitioners often determine peak intensities by ad hoc methods such as summing the number of counts in a full-width-half region about the peak of the peak or fitting parametric models to peaks in a region of interest. However, as noted in [10], the assumed parametric models are often inaccurate. In some situations, intensities of ion species that produce overlapping peaks (typically in m/z-space) can be determined with maximum likelihood methods given accurate estimates of their local isotopic abundances [11, 12, 13]. However, this peak overlap approach does not yield estimates of peaks on a fine scale over a broad range. Ideally, one should reconstruct the intensity of any ion species given the probability mass function (pmf) associated with the TOF peak of interest and the pmfs associated with neighboring peaks that affect the TOF spectrum in the re-

gion of interest. See Appendix A for a definition of the pmf associated with a particular peak.

In general, the TOF pmf for each ion of interest varies. For the case where each TOF peak is described by a translated and scaled reference TOF pmf, there are methods such as [10, 14, 15] to determine the TOF pmf. However, as far we know, there are no published methods to determine TOF pmfs at a fine scale over a broad range that vary from peak-to-peak.

Here, we determine TOF peak pmfs that that can vary from peak-to-peak with a mixture model [16, 17] (a key tool in both Machine Learning and Statistics) approach. We note that Vurpillot et al. [18] determined peak pmfs in m/z-space, but not TOF-space, with a mixture model approach where each peak is assumed to have a Gaussian shape. However the mixture model in [18] does not account for the contribution of a non-constant background to m/z measurements. Further, as noted in [18], for many atoms, peak shapes are non-Gaussian. In our approach, predicted peak pmfs can have non-Gaussian shapes, and we account for the contribution of a background to TOF measurements. We specify a collection of candidate pmfs for each peak of interest and determine their associated intensities with a maximum likelihood method. We determine candidate pmfs by a template deformation method. Hence, our approach is conceptually similar to existing deformable template methods [19, 20, 21, 22]. Based on intensities for each peak of interest determined by a maximum likelihood method, we estimate the pmf for the peak as the weighted average of its candidate pmfs. In a proof-of-principle study, we apply our method to experimental data corresponding to a silicon sample that was acquired at the National Institute of Standards and Technology (NIST). In particular, we determine the intensities of three singly charged isotopes of silicon. We expect that our method will apply to more complicated experimental cases as well. In Section 2, we discuss experimental methods and our analysis methods. In Section 3, we present our main results for a silicon sample. In Section 4, we discuss our main results and some complimentary studies.

2. Methods

2.1. Experimental method

Atom probe tomography (APT) was performed with a LEAP 4000X Si instrument (manufactured by CAMECA) operating in laser pulsing mode. Voltage pulsing mode was not performed for this work. Data were collected

from a single Si microtip residing on a Sb-doped Si microtip coupon array, which was also supplied by CAMECA. The conditions for data acquisition were as follows.

(1) Pulsed laser: the laser wavelength, energy per pulse, and repetition rate were 355 nm, 30 pJ, and 250 kHz, respectively. The pulse width is 8 ps.

(2) Analysis environment: the specimen stage was maintained at an indicated temperature of 54 K under a vacuum of approximately 7.6×10^{-9} Pa.

(3) Detection rate of ions: the detection rate was 0.003 ions per laser pulse.

(4) Span of specimen-electrode bias voltage: the data were collected over a range of bias voltage spanning from 2.75 kV to 6.77 kV. The voltage is automatically adjusted during data acquisition in order to maintain the specified detection rate. Since the specimen tip is conical with a semi-hemispherical cap, the apex diameter of the tip will increase as ions are field-evaporated away. This increasing apex diameter necessitates continuously increasing the bias voltage to maintain an electric field strength that provides the desired evaporation rate of ions.

(5) Duration of data acquisition: data were accumulated over a run time of 15.5 hours resulting in a data set composed of 40.5 million ions.

(6) Time-of-flight (TOF) mass spectrometer: the sample-to-detector flight length was 90 mm.

(7) The specimen did not fracture during data acquisition. Since we were only interested in TOF information and not 3D spatial reconstruction of the data, we did not record the comparative apex diameters nor the heights of the specimen tip before and after APT analysis.

2.2. Mixture model and reconstruction

Suppose that the mass-to-charge ratio for an ion is $r = m/z$ where m and z are the mass and charge of the ion. Further, assume that the expected number of ions with ratio r that produce counts in the observed TOF histogram is $\Theta(r)$. Assume that the conditional probability mass function for

the observed TOF histogram given r is $p_{theo}(t|r)$ where t is the midpoint of the bin. In general, $p_{theo}(t|r)$ varies with r. We model this theoretical pmf as a mixture of J candidate pmfs where the jth candidate pmf is $p(t|r,j)$, as follows:

$$p_{theo}(t|r) = \sum_j w_{r,j} p(t|r,j), \tag{2}$$

where the weights $w_{r,j}$ are non-negative and $\sum_j w_{r,j} = 1$.

Given our model assumptions, the expected number of counts in the kth TOF bin, $\mathbb{E}(n_k)$, is

$$\mathbb{E}(n_k) \;=\; \sum_r \sum_j w_{r,j} \Theta(r) p(t_k|r,j) \;+\; \lambda_b p_b(t_k), \tag{3}$$

where $p_b(t)$ is the pmf for the background process, and λ_b is the expected number of total background events. Rewriting Eq. 3, we get

$$\mathbb{E}(n_k) \;=\; \sum_r \sum_j \lambda(r,j) p(t_k|r,j) \;+\; \lambda_b p_b(t_k), \tag{4}$$

where

$$\lambda(r,j) = w_{r,j}\Theta(r). \tag{5}$$

We model the observed TOF histogram as a realization of a multivariate Poisson process where the associated Poisson random variables for the bins are independent. We determine estimates of the intensity parameters $\lambda(r,j)$ and λ_b (which are Poisson parameters in the Poisson Likelihood model) with a maximum likelihood method based on the iterative Expectation Maximization (EM) algorithm [23]. This 1D-spectrum reconstruction method (not to be confused with the method for 3D-spatial reconstruction of APT data) is mathematically similar to reconstruction methods for emission tomography [24, 25, 26](see Appendix B). To avoid possible over-fitting of our mixture model to the observed TOF spectrum, we halt the EM algorithm with a cross-validation [27] method similar to those in [28, 29]. In our cross-validation analysis, we randomly split the observed TOF spectrum into training data and validation data by a binomial thinning method (see, for example, [30]). Based on the reconstruction determined from the training data, we compute

the conditional log-likelihood function of the validation data at each iteration of the EM algorithm. When this conditional likelihood first decreases, we halt the EM algorithm. Based on cross-validation analysis of multiple splits of the observed data, we determine the median iteration (i_{med}) at which the EM algorithm is halted. We then determine a reconstruction from the observed TOF spectrum after i_{med} iterations of the EM algorithm.

Given the EM algorithm estimate of each $\lambda(r, j)$, $\hat{\lambda}(r, j)$, we estimate $\Theta(r)$ and $w_{r,j}$ as $\hat{\Theta}(r)$ and $\hat{w}_{r,j}$ where

$$\hat{\Theta}(r) = \sum_j \hat{\lambda}(r, j), \tag{6}$$

and

$$\hat{w}_{r,j} = \frac{\hat{\lambda}(r, j)}{\hat{\Theta}(r)}. \tag{7}$$

2.3. Construction of candidate pmfs

Based on an empirical estimate of the TOF pmf for the $^{28}Si^{1+}$ peak, we construct a reference pmf, $p_{ref}(t)$, where the first bin corresponds to the start time of the peak. For each of the other two peaks, we translate the reference pmf to nine possible locations in the vicinity of the nominal start time of the peak of interest. For each translation, we generate seven candidate pmfs by distorting the reference pmf as follows:

$$p_{distort}(t, \beta_i) = C_i p_{ref}^{\beta_i}(t), \tag{8}$$

where $\beta_i = 0.4 + (i - 1) * 0.2$ for $i = 1, 2, \cdots 7$, and C_i is a normalization constant that ensures the pmf sums to one. For the $^{29}Si^{1+}$ and $^{30}Si^{1+}$ peaks, we determine 63 intensity parameters for each. We determine an additional intensity parameter for the $^{28}Si^{1+}$ peak, and another for the background process. In all, we determine 128 intensity parameters.

3. Results

Based on the fully corrected TOF data (see Introduction for details about the corrections), we compute a TOF histogram where the width of each bin in 0.1 ns. We analyze a subset corresponding to TOF values in the interval [417.95, 439.95] ns (see Figure 1) corresponding to singly-charged isotopes of silicon.

We estimate a reference pmf based on analysis of the TOF spectrum associated with the $^{28}Si^{1+}$ peak. We determine a flat background by averaging TOF values in the interval [436,440] ns. The estimated background (98.7) is subtracted from the observed TOF spectrum. We fit an exponential model to the tail of the background-corrected $^{28}Si^{1+}$ peak (see Figure 2a). The observed values in the region of the exponential fit (thick red line in Figure 2a) are replaced by the exponential model prediction. We normalize the extrapolated version of the Figure 2a spectrum to get a reference pmf that sums to 1 for relative TOF values up to 1000 ns. We generate candidate pmfs from this reference pmf according to Eq. 8. We normalize each candidate pmf so that it sums to 1 (see Figure 2b). We determine a nominal start time for the $^{29}Si^{1+}$ peak as the nominal start time of the $^{28}Si^{1+}$ peak plus the difference between the TOF time where the $^{29}Si^{1+}$ takes it maximum value and TOF time where the $^{28}Si^{1+}$ peak takes its maximum value. A similar method yields a nominal start time for the $^{30}Si^{1+}$ peak.

Given n counts in a particular bin of the TOF histogram, the number of thinned counts in the same particular bin of the training data, n_{train}, is a realization of Binomial random variable with parameters n and p. Here, we set $p = 0.8$. Given n_{train}, the number of thinned counts in the same particular bin in the validation data is $n - n_{train}$. For each of five sets of training and validation data, we determine estimates of the 128 Poisson parameters in our model (see Section 2.2) from the training data with the EM algorithm. At each iteration of the EM algorithm, we compute the conditional log-likelihood of the validation data based on the Poisson parameters determined from the training data. When this conditional log-likelihood first decreases, we halt the EM algorithm. Based on analysis of the five sets of training and validation data, we determine the median iteration at which the EM algorithm is halted to be $i_{med} = 33\ 753$. From the original TOF histogram, we determine Poisson parameters with EM algorithm after i_{med} iterations. In our implementation of the EM algorithm, the initial value of the Poisson parameter for each candidate pmf (excluding the background pmf) is the sum of counts in the observed histogram divided by 127. The initial value of the background intensity is $99 * n_{bin} * f$ where f if 0.8 for training data produced by thinning, f is 1 for the observed TOF histogram, and n_{bin} is the number of bins (221) in each TOF histogram.

In Figures 3 and 4, for the $^{29}Si^{1+}$ and $^{30}Si^{1+}$ peaks, for each candidate translation, we display the estimated intensity for each of seven candidate pmfs. In Figure 5a, for the $^{29}Si^{1+}$ peak, for each candidate translation, we

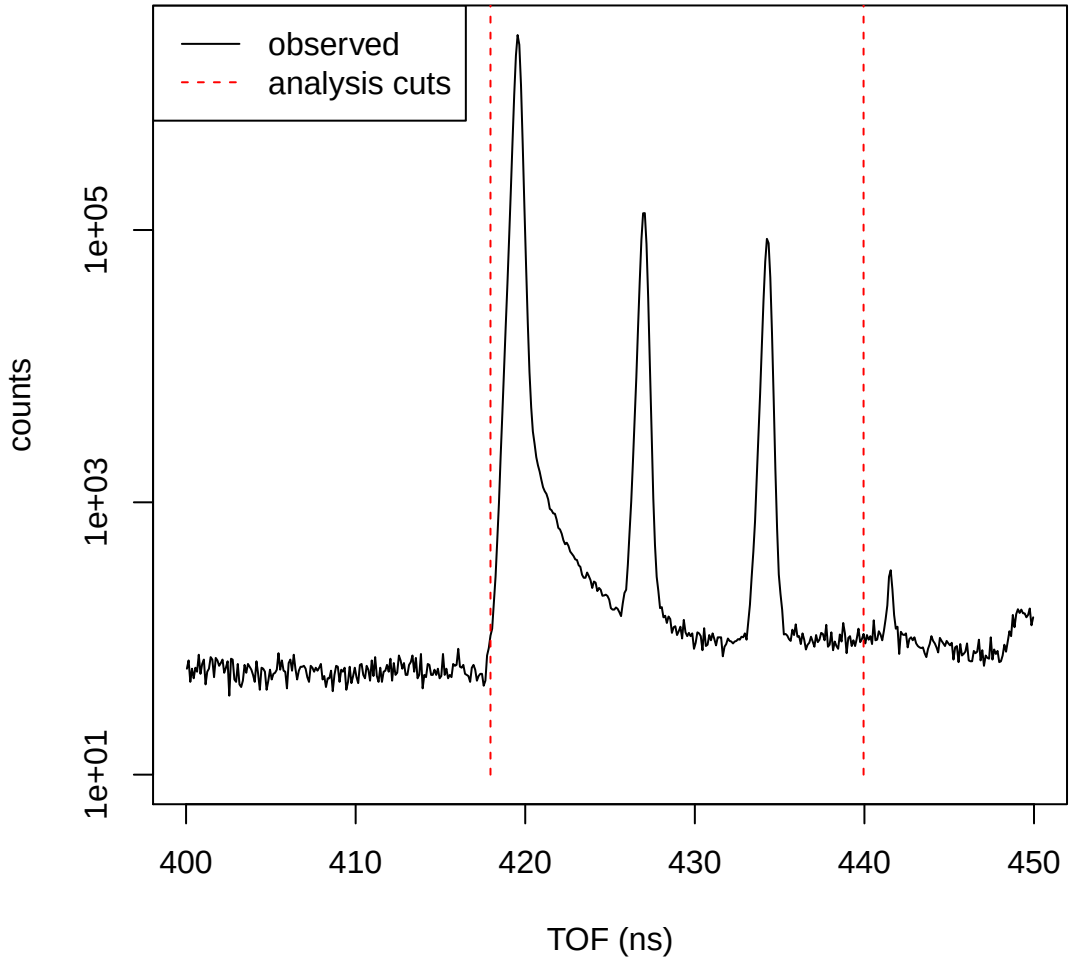

Figure 1: Observed TOF spectra for a silicon sample. The three peaks inside the analysis region (from 419.95 ns to 439.95 ns) are due to singly charged isotopes of silicon– $^{28}Si^{1+}$, $^{29}Si^{1+}$, and $^{30}Si^{1+}$. There are 221 bins with width of 0.1 ns. From count data corresponding to TOF values in the interval [436,440] ns, we determine the background to be 98.7 counts.

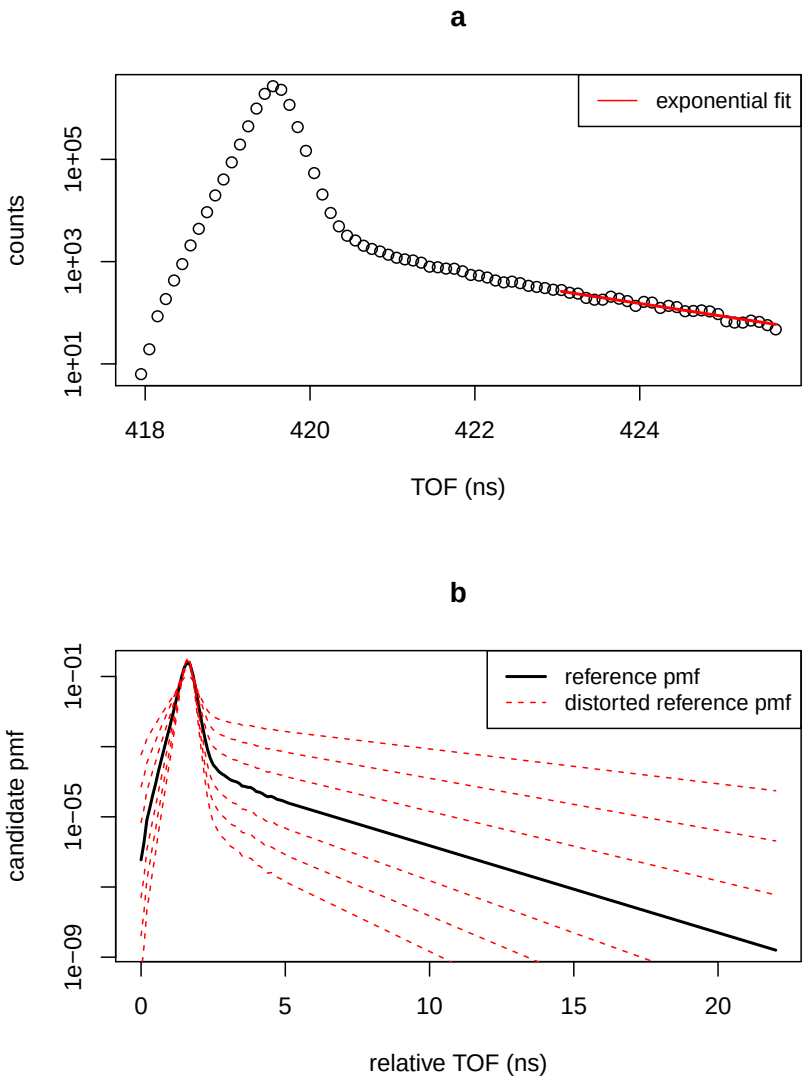

Figure 2: In (a), we fit an exponential model to the background-corrected data produced by the $^{28}Si^{1+}$ peak. (The fitted value of the mean lifetime of the exponential and its standard uncertainty are $\tau = 1.75$ ns and 0.09 ns.) Based on the estimated exponential model parameters, we extrapolate to arbitrarily large values of TOF. Based on the extrapolated curve in (a), we determine a reference pmf. In (b), based on Eq. 8, we generate candidate pmfs by deforming the reference pmf.

plot the sum of the seven intensities. In Figure 5b, for the $^{30}Si^{1+}$ peak, for each candidate translation, we plot the sum of the seven intensities. Based on Eq. 6, the overall intensity for the $^{29}Si^{1+}$ peak is the sum of the 63 intensities shown in Figure 3. Similarly, the overall intensity for the $^{30}Si^{1+}$ peak is the sum of the 63 intensities shown in Figure 4.

In Figure 6, we compare observed and predicted TOF spectra and show standardized residuals. In Figure 7, we compare the contribution of each peak to the overall TOF spectrum. In Figure 8, we compare the shapes of the pmfs for the three peaks. In Table 1, we list estimated intensities for each peak and the estimated isotopic abundance associated with each isotope of silicon.

Table 1: Below, we show estimates of intensities and associated isotopic abundances for for $^{28}Si^{1+}$, $^{29}Si^{1+}$ and $^{30}Si^{1+}$ determined at 33 753 iterations of the iterative EM algorithm. This halting iteration is determined by cross-validation. The theoretical values for isotopic abundances of ^{28}Si, ^{29}Si, and ^{30}Si are 0.9222, 0.0469 and 0.0309. For iterations of EM algorithm greater than 10 000 iterations, results agree to the number of significant digits shown below.

peak	intensity	isotopic abundance
$^{28}Si^{1+}$	1.05549E+07	0.92121
$^{29}Si^{1+}$	5.517E+05	0.04815
$^{30}Si^{1+}$	3.511E+05	0.03064

4. Discussion

4.1. Reconstruction method and Poisson model

As discussed earlier, we assume that the observed TOF histogram is a realization of a multivariate Poisson process. Visual inspection of the 146 standardized residuals computed according to the Poisson model (see Figure 6b) at times beyond the nominal start time of the $^{29}Si^{1+}$ peak suggests that our Poisson model and reconstruction method are reasonable. Further, the fact that the root-mean-square (RMS) value of these 146 standardized residuals is 1.08 suggests that our Poisson model and reconstruction method are reasonable. We note that standardized residuals for early times of the $^{28}Si^{1+}$ peak are generally smaller in magnitude compared to the magnitude of standardized residuals at later times. We attribute this to the fact that the assumed pmf values for the $^{28}Si^{1+}$ peak at early times are proportional to background-corrected observed values.

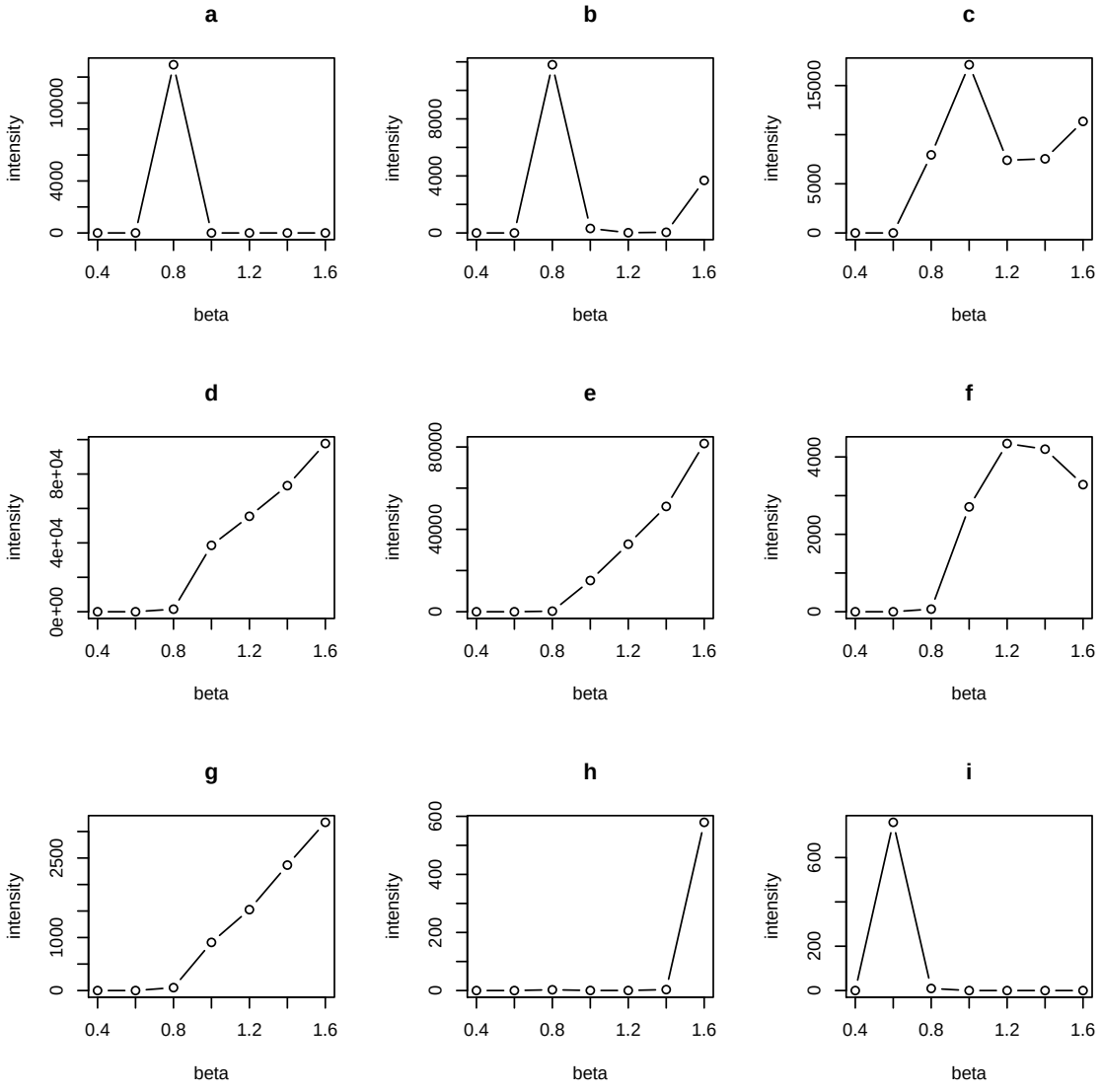

Figure 3: For the $^{29}Si^{1+}$ peak, we show intensities of candidate pmfs determined with the EM algorithm after 33 753 iterations (determined by cross-validation). For each candidate translation about the nominal start time of the $^{29}Si^{1+}$ peak, (-0.4, 0.3, 0.2, 0.1, 0, 0.1, 0.2, 0.3 ,0.4) ns, we show intensities for the seven candidate pmfs in plots ("a", "b", "c", "d", "e", "f", "g", "h", "i").

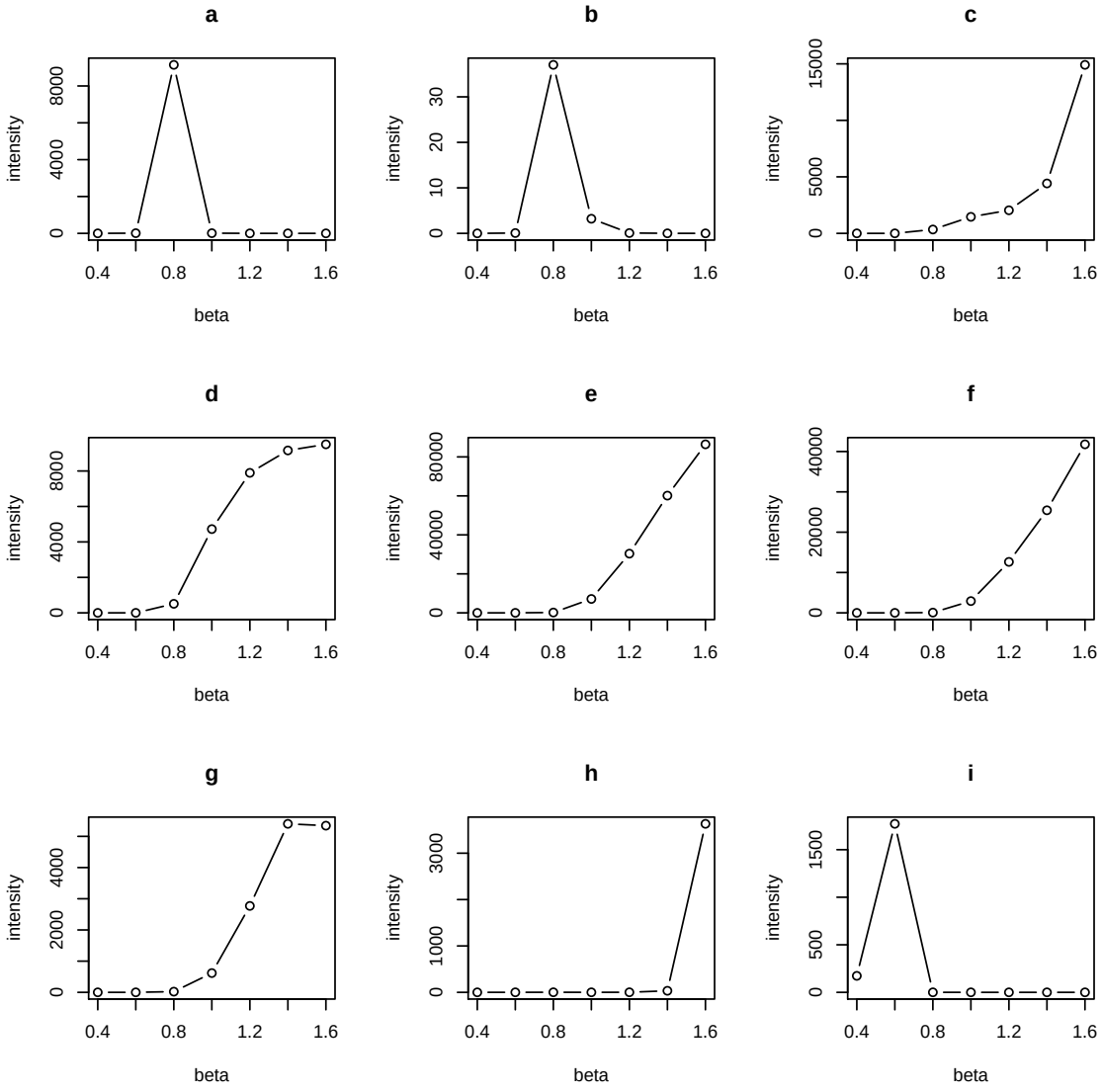

Figure 4: For the $^{30}Si^{1+}$ peak, we show intensities of candidate pmfs determined with the EM algorithm after 33 753 iterations (determined by cross-validation). For each candidate translation about the nominal start time of the $^{30}Si^{1+}$ peak, (-0.4, 0.3, 0.2, 0.1, 0, 0.1, 0.2, 0.3 ,0.4) ns, we show intensities for the seven candidate pmfs in plots ("a", "b", "c", "d", "e", "f", "g", "h", "i").

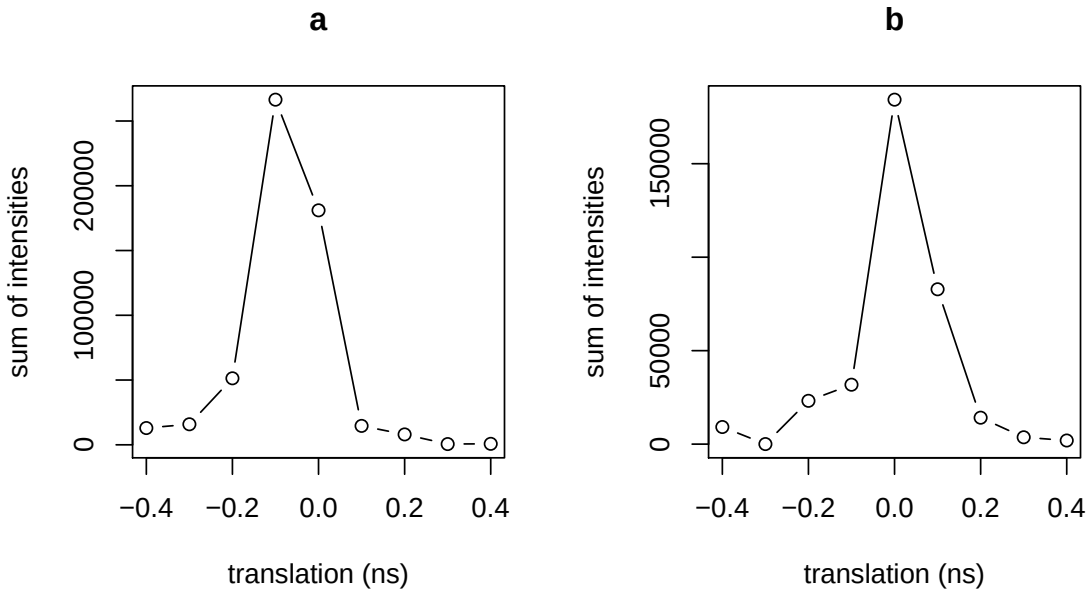

Figure 5: In (a) and (b), we show the sum of the intensities of the seven candidate pmfs for each candidate translation for the $^{29}Si^{1+}$ peak and the $^{30}Si^{1+}$ peak respectively.

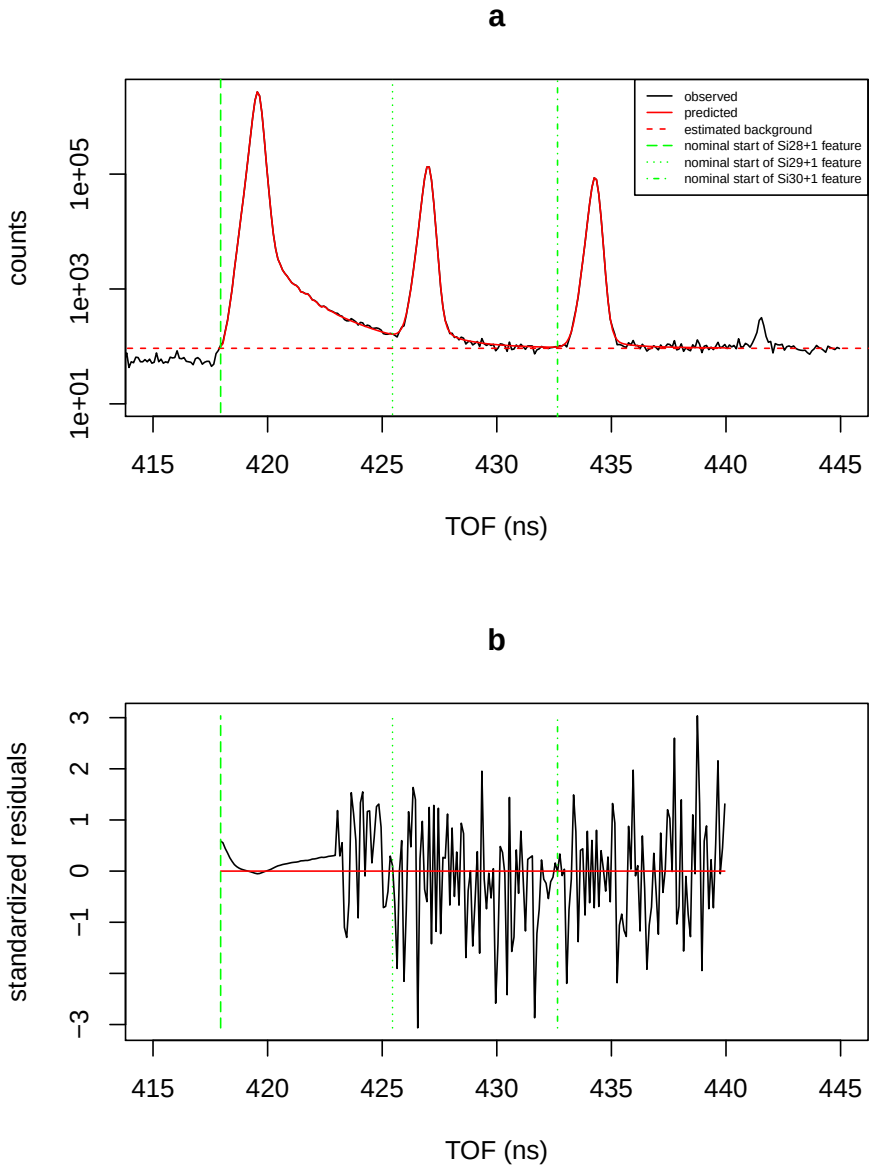

Figure 6: (a):Observed and predicted TOF spectra. The EM algorithm determines the background to be 92.7 counts for results in the analysis region (see Figure 1). (b): Standardized residuals according to our Poisson model (difference between observed and predicted values divided by the estimated standard deviation of the observation (the square root of the predicted value)). The root-mean-square (RMS) value of the 146 standardized residuals corresponding to TOF values as large or larger than the nominal start time of the $^{29}Si^{1+}$ peak is 1.08.

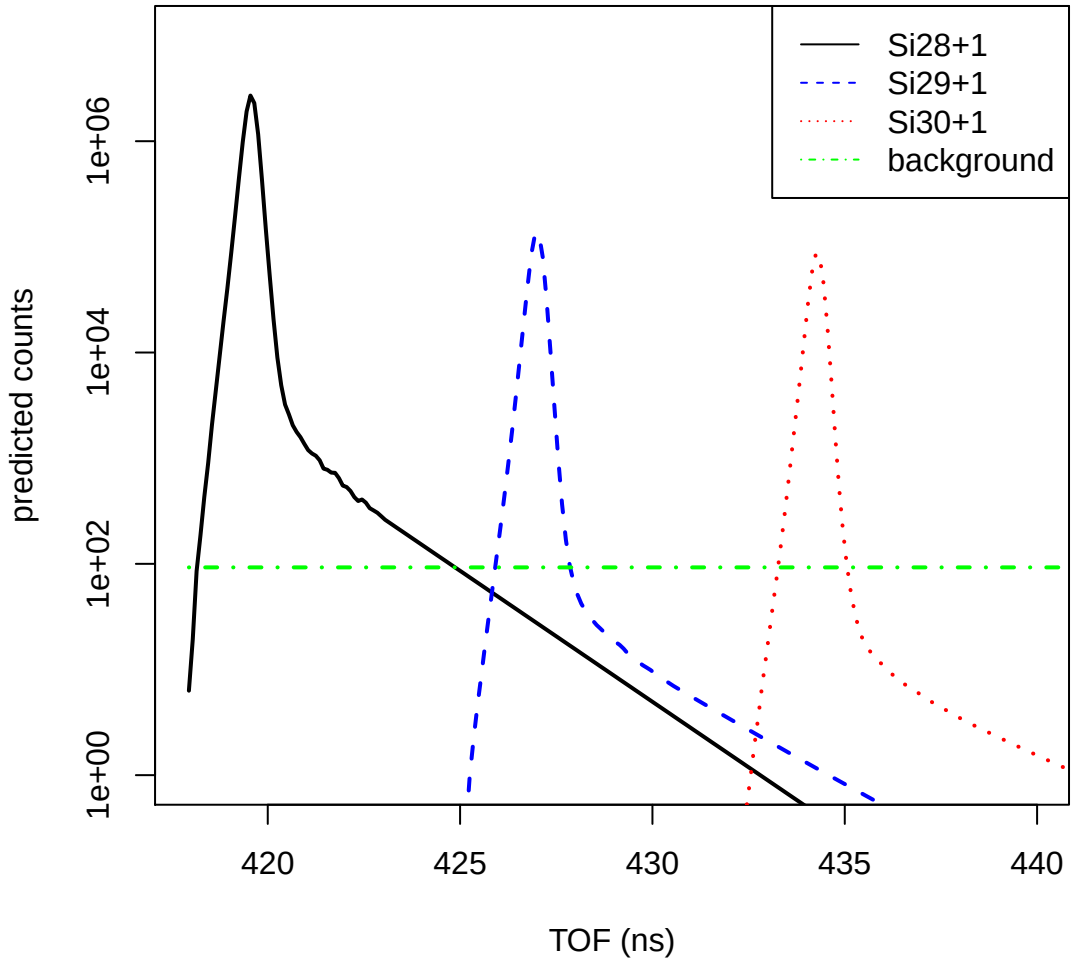

Figure 7: Contributions of the ($^{28}Si^{1+}$, $^{29}Si^{1+}$, $^{30}Si^{1+}$) peaks and the background (92.7 counts) to the overall TOF spectrum predicted by our mixture model analysis.

Our reconstruction method conserves counts. That is, the sum of observed counts in all bins and the sum of predicted counts in all bins agree.

In our model, the observed number of counts in the kth TOF histogram bin, n_k, is a realization of a Poisson process with expected value λ_k. Given that the sum of observed counts in all K bins is n, it is well-known (see, for example, [40]) that $(X_1, X_2, \ldots X_K)$ is a multinomial random variable with the following distribution (probability mass function)

$$\Pr(X_1 = n_1, X_2 = n_2, \ldots X_K = n_K | X = n) = \frac{n!}{n_1! n_2! \ldots n_K!} \prod_{k=1}^{K} p_k, \qquad (9)$$

where $X = X_1 + X_2 \ldots X_K$, and

$$p_k = \frac{\lambda_k}{\lambda_1 + \lambda_2 + \ldots \lambda_K}. \qquad (10)$$

4.2. Stability of estimates

In a stability study, we determine results with the EM algorithm for iterations ranging from 1000 to 4 million. As discussed earlier, the overall intensity estimates for the $^{29}Si^{1+}$ peak and the $^{30}Si^{1+}$ peak are the sum of estimated intensities determined for each of 63 candidate pmfs (see Eq. 6). After 10 000 iterations, the estimate of the intensity of the $^{29}Si^{1+}$ peak and the estimate of the $^{30}Si^{1+}$ peak are both stable to within four significant digits. After 10 000 iterations, the estimate of the intensity of the $^{28}Si^{1+}$ peak is stable to within six significant digits. For either the $^{29}Si^{1+}$ or $^{30}Si^{1+}$ peak, in general, the intensity associated with any one of the 63 candidate pmfs is not stable to within four digits after 10 000 iterations. For instance, for the $^{29}Si^{1+}$ peak, the ratios of the intensity estimates for candidate pmfs at 4 million iterations and i_{med} iterations range from 2.7E-320 to 14.3. For the $^{30}Si^{1+}$ peak, the ratios range from 1.5E-321 to 6315. One expects the average of the 63 intensities for each peak to be better determined than any one of the 63 estimates corresponding to that peak. In medical imaging studies, a similar phenomenon occurs when EM algorithm estimates of a large number of spatially varying Poisson parameter estimates are averaged within regions of interest (for example, see [31, 32]). Estimates of the predicted $^{29}Si^{1+}$ and $^{30}Si^{1+}$ peaks. at any particular TOF value are less stable than overall intensities of these peaks (see Figure 9).

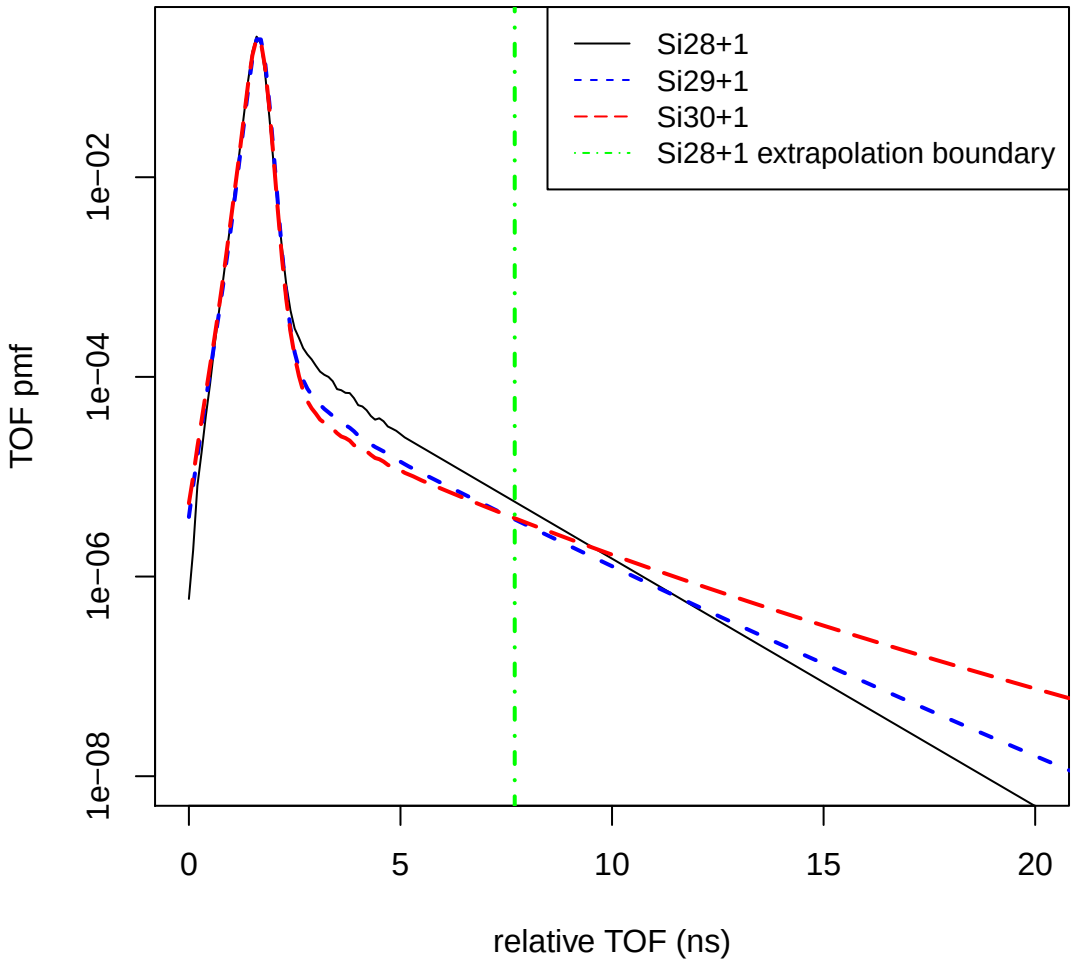

Figure 8: Comparison of aligned estimated probability mass functions for the ($^{28}Si^{1+}$, $^{29}Si^{1+}$, $^{30}Si^{1+}$) peaks determined with EM algorithm after 33 753 iterations (determined by cross-validation).

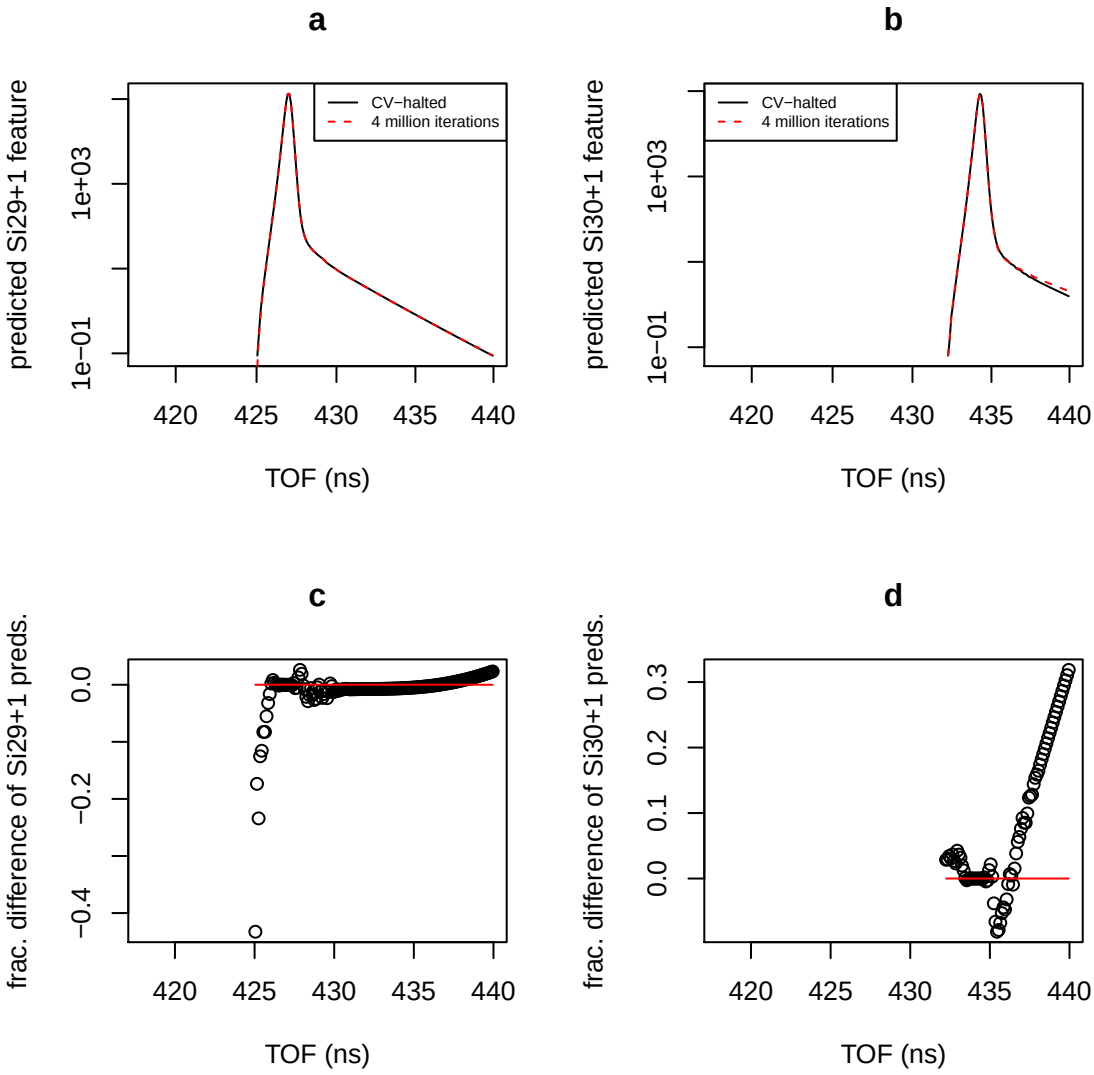

Figure 9: (a) Comparison of predicted $^{29}Si^{1+}$ peak determined by the EM algorithm after 33 753 iterations (determined by cross-validation) and 4 million iterations. (b) Comparison of predicted $^{30}Si^{1+}$ peak determined by the EM algorithm after 33 753 iterations and 4 million iterations. (c) Fractional difference between predictions shown in (a). (d) Fractional difference between predictions shown in (b).

4.3. Initial values of Poisson parameter estimates

When the initial values of the Poisson parameter estimates in the EM algorithm method are equated to the square root of the values assumed in our main study, for i_{med} iterations, the estimated value of the estimated 128 Poisson parameters are similar. The ratios of the new and original estimates of the Poisson parameters vary from 0.93 to 1.01, and the median ratio is 1.00. The fractional differences between the predicted value of the TOF spectrum with new initial value relative to the predicted value determine with the original initial values ranges from -2.1E-05 to 1.3E-05 (over all bins). Further, the estimates of the intensities (determined with the original and revised choice of initial values of the Poisson parameters) for the $^{28}Si^{1+}$ $^{29}Si^{1+}$ and $^{30}Si^{1+}$ peaks agreed to within nine significant digits, six significant digits, and six significant digits respectively.

4.4. Background jumps

Our comparison of predicted and observed TOF spectra shown in Figure 6a strongly suggests that the background rate before the start of the $^{28}Si^{1+}$ peak is less than the background rate after the start of the $^{28}Si^{1+}$ peak. The source of this jump could be an ion feedback (IFB) artifact produced by micro-channel plates (MCPs) in the single ion detection systems [34, 35, 36, 37, 38, 10].

4.5. Peak-to-peak pmf variation

Our results appear consistent with the hypothesis that the TOF pmfs vary among the three peaks (see Figure 8). As a caveat, the source of this apparent variation among the pdfs could be due to the physics of ion evaporation or systematic effects associated with multiple-hit events [33], IFB artifacts, or perhaps other instrumental effects.

4.6. Extrapolation model

In our analysis, we model the upper tail of the $^{28}Si^{1+}$ peak as an exponential (see Figure 2). While this model appears to be reasonable, we can not rule out the possibility that a non-exponential model is more accurate.

4.7. Application to other experimental data

In our study, the peaks due to $^{28}Si^{1+}$, $^{29}Si^{1+}$, $^{30}Si^{1+}$, overlap, but peaks that are not in analysis region appear to not significantly overlap with the silicon peaks. If other peaks beyond the analysis had significantly overlapped with the silicon peaks, we should account for the contribution of these peaks. We believe that our mixture model approach is flexible enough to model the contributions of such peaks. For other applications, the method to generate candidate pmfs may be different than the method presented here. For instance, for peaks with shapes that vary more dramatically (see, for example, [41]) than the peaks considered in this work, the number of candidate pmfs for each peak might be larger than assumed in this work and analysis could be more computer intensive. Due to the flexibility of our method, it may be possible to determine candidate peak pmfs from deformations of analytical models. Scaling up the mixture model analysis to a larger subset of the observed TOF spectrum is a worthwhile topic for future research.

4.8. Uncertainties

Quantifying uncertainties for results is a worthy topic for future research.

5. Conclusions

We presented a mixture model method to determine TOF pmfs that can vary from peak-to-peak. In a proof-of-principle study based on experimental data, we demonstrated the feasibility of our method by determining a TOF pmf, intensity and isotopic abundance for each of three singly charged isotopes of silicon. How well our method works for more complicated examples is a topic for future study.

Appendix A: Probability mass function

Consider an ideal experiment where time-of-flight measurements are produced by ions of the same species. Further, assume that each time-of-flight measurement is a realization of a random variable T. Suppose that we represent the TOF spectrum associated with this ion species as a histogram with K bins where K can be arbitrarily large. Further, suppose that the probability that any realization of T falls in the kth bin is $f(k)$. Since T is a random variable, the bin index is a random variable $g(T)$ where g is a known

function that determines the bin index given the realization of T. We denote the probability that $g(T) = k$ as

$$\Pr(g(T) = k) = f(k), \tag{A.1}$$

where $k = 1, 2, \ldots K$. Given that $\sum_{k=1}^{K} f(k) = 1$, $f(k)$ is a probability mass function. In this work, $K = 10\ 000$ for each pmf of interest. For this large value of K, we assume that $\sum_{k=1}^{K} f(k) = 1$. As discussed in many references (see, for example, [39]), the probability mass function is sometimes referred to as a discrete density function or probability function. In our study, we seek to determine pmfs associated with different ion species that can vary from species-to-species, as well as the intensity for each peak.

Appendix B: EM algorithm applied to APT

Following the nomenclature in [24] and [25], we assign an integer index b to each of the Poisson parameters in our model (see Section 2.2) (where $b = 1, 2 \cdots B$) and an integer index d (where $d = 1, 2 \cdots D$) to each bin of the TOF histogram. In our study, $B = 128$ and $D = 221$. The Poisson likelihood of the observed TOF histogram $\mathbf{n} = (n_1, n_2, \cdots n_D)$ given the associated Poisson parameters (intensities) for the candidate pmfs $\lambda = (\lambda(1), \lambda(2) \cdots \lambda(B))$ is

$$L(\mathbf{n}|\lambda) = \prod_{d=1}^{D} \frac{e^{-\lambda^*(d)} \lambda^*(d)^{n(d)}}{n(d)!}, \tag{B.1}$$

where the mean of $n^*(d)$ is

$$\lambda^*(d) = \sum_{b=1}^{B} \lambda(b) p(b, d), \tag{B.2}$$

and $p(b, d)$ is the probability that the observed TOF will fall into the dth TOF histogram bin predicted by the bth pmf.

The EM algorithm is an iterative scheme for determination of maximum likelihood estimates of the Poisson parameters. The bth Poisson parameter, $\hat{\lambda}$, is updated as follows:

$$\hat{\lambda}(b)^{new} = \frac{\hat{\lambda}(b)^{old}}{p(b, .)} \sum_{d=1}^{D} \frac{n(d) p(b, d)}{\sum_{b'=1}^{B} \hat{\lambda}(b')^{old} p(b', d)}, \tag{B.3}$$

where $p(b,.) = \sum_{d=1}^{D} p(b,d)$. For more technical details on how to derive Eq. B.3, see Section 2 of [25]. Shepp and Vardi [24] proved that, after each iteration of the EM algorithm, the likelihood of the data never decreases provided that the initial estimates are positive.

In our study, we estimate the expected background contribution to each TOF measurement. For the case where the expected background contribution is treated as known, one can derive an EM algorithm (see, for example, Fessler and Hero [42]) similar to Eq. B.3

Acknowledgments We thank B. Caplins, F. Meisenkothen and A. Pintar of NIST for helpful comments. Contributions of staff of NIST, an agency of the US Government are not subject to copyright in the US. Certain commercial equipment, instruments, or materials are identified in this paper to foster understanding. Such identification does not imply recommendation or endorsement by the National Institute of Standards and Technology, nor does it imply that the materials or equipment identified are necessarily the best available for the purpose.

Author Contributions Norman Sanford acquired the raw APT measurements at NIST and processed them to yield the TOF measurements analyzed here. He also contributed text on the APT method and experimental details. Kevin Coakley developed the reconstruction method and associated software to reconstruct TOF measurements. He also analyzed results and was the primary author of the manuscript. Both authors have approved the final article for publication.

Declaration of Competing Interest The authors declare that they have no known competing financial interests or personal relationships that could have appeared to influence the work reported in this paper.

Funding This research did not receive any specific grant from funding agencies in the public, commercial, or not-for-profit sectors.

Data Availability Data underlying the results presented in this paper are not publicly available at this time but may be obtained from the authors upon reasonable request.

References

[1] B. Gault, M. P. Moody, J. M. Cairney, S. P. Ringer, Atom Probe Microscopy, Vol. 160 of Springer Series in Materials Science, Springer New York, New York, NY, 2012.

[2] D. J. Larson, T. J. Prosa, R. M. Ulfig, B. P. Geiser, T. F. Kelly, Local Electrode Atom Probe Tomography, Springer New York, New York, NY, 2013.

[3] M. K. Miller, R. G. Forbes, Atom-Probe Tomography, Springer US, Boston, MA, 2014.

[4] C. Pareige, W. Lefebvre-Ulrikson, F. Vurpillot, X. Sauvage, Atom Probe Tomography, Elsevier, Cambridge, MA, 2016.

[5] A. Devaraj, D.E. Perea, J. Liu, L.M. Gordon, T.J. Prosa, P. Parikh, D.R. Diercks, S. Meher, R.P. Kolli, Y.S. Meng and S. Thevuthasan (2018). Three-dimensional nanoscale characterisation of materials by atom probe tomography. International Materials Reviews, 63(2), pp.68-101.

[6] B.W. Caplins, P.T. Blanchard, A.N. Chiaramonti, D.R. Diercks, L. Miaja-Avila, and N.A. Sanford (2020). An algorithm for correcting systematic energy deficits in the atom probe mass spectra of insulating samples. Ultramicroscopy, 213, 112995.

[7] N.A. Sanford, P.T. Blanchard, M. Brubaker, K.A. Bertness, A. Roshko, J.B. Schlager, R. Kirchhofer,D. R. Diercks, B. Gorman, (2014). Laser-assisted atom probe tomography of MBE grown GaN nanowire heterostructures. physica status solidi (c), 11(34), 608-612. https://doi.org/10.1002/pssc.201300579

[8] Q. Zhang, B. Klein, N.A. Sanford, et al. Comparative Apex Electrostatics of Atom Probe Tomography Specimens. Journal of Elec Materi 50, 30223029 (2021). https://doi.org/10.1007/s11664-021-08932-6

[9] https://www.cameca.com/service/software/ivas

[10] F. Meisenkothen, D.V. Samarov, I. Kalish, and E.B. Steel (2020). Exploring the accuracy of isotopic analyses in atom probe mass spectrometry. Ultramicroscopy, 216, p.113018.

[11] A.J. London, D. Haley and M.P. Moody (2017). Single-ion deconvolution of mass peak overlaps for atom probe microscopy. Microscopy and Microanalysis, 23(2), pp.300-306.

[12] A.J. London (2019). Quantifying uncertainty from mass-peak overlaps in atom probe microscopy. Microscopy and Microanalysis, 25(2), pp.378-388.

[13] J. Keutgen, A.J. London and O. Cojocaru-Mirdin (2021). Solving peak overlaps for proximity histogram analysis of complex interfaces for atom probe tomography data. Microscopy and Microanalysis, 27(1), pp.28-35.

[14] L.J.S. Johnson, M. Thuvander, K. Stiller, M. Oden, L. Hultman (2013), Blind deconvolution of time-of-flight mass spectra from atom probe Ultramicroscopy, 132, pp. 60-64.

[15] F. Meisenkothen, D. Samarov, M. McLean, I. Kalish, and E. Steel (2021). Adaptive Peak Fitting for Isotope Analysis via Atom Probe Mass Spectrometry. Microscopy and Microanalysis, 27(S1), pp.176-177.

[16] G.J. McLachlan, S.X. Lee and S.I. Rathnayake (2019). Finite mixture models. Annual review of statistics and its application, 6, 355-378.

[17] G.J. McLachlan and D. Peel (2004). Finite Mixture Models, Wiley Series in Probability and Statistics.

[18] F. Vurpillot, C. Hatzoglou, B. Radiguet, G. Da Costa,F. Delaroche and F. Danoix (2019). Enhancing element identification by expectationmaximization method in atom probe tomography. Microscopy and Microanalysis, 25(2), pp.367-377.

[19] Y. Amit, U. Grenander, and M. Piccioni (1991). Structural image restoration through deformable templates. Journal of the American Statistical Association, 86(414), 376-387.

[20] A.L. Yuille, P.W. Hallinan and D.S. Cohen (1992). Feature extraction from faces using deformable templates. International journal of computer vision, 8(2), 99-111.

[21] A.K. Jain, Y. Zhong and S. Lakshmanan (1996). Object matching using deformable templates. IEEE Transactions on pattern analysis and machine intelligence, 18(3), pp.267-278.

[22] A.V. Dalca, M. Rakic, J. Guttag, and M.R. Sabuncu (2019). Learning conditional deformable templates with convolutional networks. arXiv preprint arXiv:1908.02738.

[23] A.P. Dempster, N.M. Laird and D.B. Rubin (1977). Maximum likelihood from incomplete data via the EM algorithm. Journal of the Royal Statistical Society: Series B (Methodological), 39(1), 1-22.

[24] L. A. Shepp and Y. Vardi (1982), Maximum Likelihood reconstruction for emission tomography, IEEE Transactions on Medical Imaging Volume 1, Issue 2, pp. 113-122.

[25] Y.Vardi, L.A. Shepp, and L. Kaufman (1985), A statistical model for positron emission tomography. Journal of the American statistical Association, 80(389), 8-20.

[26] K. Lange and R. Carson (1984). EM reconstruction algorithms for emission and transmission tomography. J Comput Assist Tomogr, 8(2), pp.306-16.

[27] J. Friedman, T. Hastie,and R. Tibshirani (2001). The elements of statistical learning (Vol. 1, No. 10). New York: Springer series in statistics.

[28] K.J. Coakley (1991). A cross-validation procedure for stopping the EM algorithm and deconvolution of neutron depth profiling spectra. IEEE Transactions on Nuclear Science, 38(1), 9-15.

[29] K.J. Coakley and J. Llacer (1991). Use of cross-validation as a stopping rule in emission tomography image reconstruction. In Medical Imaging V: Image Physics (Vol. 1443, pp. 226-233). International Society for Optics and Photonics.

[30] J. Llacer, E. Veklerov, K.J. Coakley, E.J. Hoffman and J. Nunez (1993) Statistical analysis of maximum likelihood estimator images of human brain FDG PET studies, In IEEE Transactions on Medical Imaging, vol. 12, no. 2, pp. 215-231, June 1993

[31] R.E. Carson, Y. Yan, B. Chodkowski, T. K. Yap, and M. E. Daube-Witherspoon (1994). Precision and accuracy of regional radioactivity quantitation using the maximum likelihood EM reconstruction algorithm. IEEE transactions on medical imaging, 13(3), 526-537.

[32] W. Xia, S.J. Glick, T.S. Pan, E.J. Soares, and D.S. Luo (1997). Region of interest evaluation of SPECT image reconstruction methods using a realistic brain phantom. IEEE Transactions on Nuclear Science, 44(3), 1336-1341.

[33] F. Meisenkothen, E.B. Steel, T.J. Prosa, K.T. Henry and R.P. Kolli (2015) Effects of detector dead-time on quantitative analyses involving boron and multi-hit detection events in atom probe tomography, Ultramicroscopy 159 (Part 1) pp. 101111.

[34] J.L. Wiza (1979), Microchannel plate detectors, Nucl. Instrument. Methods 162

[35] K. Oba, P. Rehak (1981) Studies of high-gain micro-channel plate photomultipliers, IEEE Trans. Nucl. Sci. NS-28 pp. 683688.

[36] M. Liptak, W.G. Sandie, E.G. Shelley, D.A. Simpson (1984) Microchannel plate electron multiplier for mass spectrometer applications IEEE Trans Nucl Sci, NS-31, pp. 780-785

[37] D.M. Murphy and K. Mauersberger (1985) Operation of a microchannel plate counting system in a mass spectrometer, Rev. Sci. Instrument. 56 (1985) 220226.

[38] M. Muller, T. Mikoviny, A. Wisthaler (2014) Detector aging induced mass discrimination and non-linearity effects in PTR-ToF-MS, Int. J. Mass Spectrom. 365-366 9397.

[39] A. Mood, F.A. Graybill and D.C. Boes (1974).A Introduction to the theory of statistics, McGraw Hill.

[40] G. Last and M. Penrose, M. (2017). Lectures on the Poisson process (Vol. 7). Cambridge University Press.

[41] A.Sen, M. Bachhav, F. Vurpillot, J.M. Mann, P.K. Morgan,T.A. Prusnick,and J.P. Wharry (2021) Influence of field conditions on quantitative analysis of single crystal thorium dioxide by atom probe tomography. Ultramicroscopy, 220, p.113167.

[42] J.A. Fessler and A.O. Hero (1994). Space-alternating generalized expectation-maximization algorithm. IEEE Transactions on signal processing, 42(10), pp.2664-2677.